

Research Article

Experimental Study on the Influence of Specimen Shape on Rockburst Proneness of Red Sandstone

Jiajun Yang,¹ Fengqiang Gong ,^{1,2,3} Dongqiao Liu,² and Zhixiang Liu¹

¹School of Resources and Safety Engineering, Central South University, Changsha 410083, China

²State Key Laboratory for Geomechanics and Deep Underground Engineering, China University of Mining and Technology, Beijing 100083, China

³School of Civil Engineering, Southeast University, Nanjing 211189, China

Correspondence should be addressed to Fengqiang Gong; fengqiangg@126.com

Received 9 February 2020; Revised 24 June 2020; Accepted 28 July 2020; Published 17 August 2020

Academic Editor: Caiping Lu

Copyright © 2020 Jiajun Yang et al. This is an open access article distributed under the Creative Commons Attribution License, which permits unrestricted use, distribution, and reproduction in any medium, provided the original work is properly cited.

To investigate the specimen shape effect on rockburst proneness of rock materials, a string of conventional and single-cycle loading-unloading uniaxial compression tests was performed with cylindrical and cuboid red sandstone specimens. Despite similar development paths on stress-strain curves for the specimens with two shapes, the cuboid specimens generally show a higher uniaxial compressive strength than the cylindrical specimens. The energy evolution laws inside the two shaped specimens were explored. The results show that the input energy density (IED), elastic energy density (EED), and dissipated energy density (DED) of the two shaped specimens increased in a quadratic relationship with the increment of unloading level. Moreover, the linear relationships between the EED, DED, and IED were further confirmed for two shaped specimens, which were defined as the linear energy storage and dissipation laws, respectively. The energy storage coefficients and energy dissipation coefficients (the slopes of the linear relationships between the EED, DED, and IED, respectively) are almost independent of the specimen shape. According to the linear energy storage and dissipation laws, the peak EED and peak DED of every specimen can be calculated accurately. Finally, combining the failure process of rock specimens recorded by a high-speed camera, the elastic energy index (W_{ET}), the residual elastic energy index (A_{EF}), and the far-field ejection mass ratio (M_F) of each specimen were adopted to assess the rockburst proneness of the red sandstone sampled in cylindrical and cuboid. The results show that cuboid specimens exhibited stronger rockburst proneness than cylindrical ones, which favorably agreed with the actual failure phenomena.

1. Introduction

With the underground engineering developing to the deeper crustal areas, rockburst phenomena appear with a growing trend which pose a vast risk to mining operations and result in production losses [1–7]. Hence, scholars in mounting number begin to focus on rockburst problems [8–13], and the rockburst proneness turned into one of the vital research sites [14–16]. Moreover, because the deformation and failure of rock are accompanied by energy conversion, rockburst is often caused by energy release [17]. Some scholars analyzed the rockburst proneness of rock materials from an energy perspective, and many rockburst proneness criteria were proposed and developed. For example, Kidybiński [18]

introduced the strain energy storage index W_{ET} with the single-cycle loading-unloading uniaxial compression (SCLUC) test, which has been widely used to assess the rockburst proneness of rock materials [19–23]; Wang and Park [20] investigated and predicted the intensity of the rockburst proneness of Linglong gold mine in China adopting the elastic strain energy PES; Based on the linear energy storage law, Gong et al. [16, 24] presented the peak-strength strain energy storage index W_p^{ET} and the residual elastic energy index A_{EF} . Among the above references, all of these rockburst proneness criteria were obtained with cylindrical specimens. However, in many cases, cuboid specimens were often used when investigating rock behavior under complex stress states such as biaxial and true triaxial

compression tests [25, 26]. Although several researchers have revealed the shape effect on the mechanical properties of rock specimens under the conventional uniaxial compression (UC) tests [27, 28], the studies on rockburst proneness of cuboid specimens were relatively rare.

In this paper, to investigate the effect of specimen shape on rockburst proneness, the SCLUC tests were implemented with the specimens of two shapes (cylinder and cuboid), and the input energy density (IED), elastic energy density (EED), and dissipated energy density (DED) were calculated by the graphical integration according to the stress-strain curves at different unloading points. According to the test results, the energy evolution laws inside the two shaped specimens were attained. Meanwhile, combined with the bursting processes of specimens accorded by a high-speed camera, the rockburst proneness of the cylindrical and cuboid specimens was compared by the elastic energy index (W_{ET}), the residual elastic energy index (A_{EF}), and the far-field ejection mass ratio (M_F).

2. Specimens and Methods

2.1. Specimen Preparation. The red sandstone block collected from the Shandong Province of China was used for testing. To compare the effect of specimen shape on the determination of rockburst proneness, the cylindrical and cuboid specimens with sizes of $\Phi 50 \times 100$ mm and of $50 \times 50 \times 100$ mm were prepared according to the guidelines of International Society for Rock Mechanics (ISRM). The cylindrical specimens were named as RS-CL, such as RS-CL-1; the cuboid specimens were named as RS-CB, such as RS-CB-1. The basic parameters of specimens were measured and are presented in Table 1.

2.2. Test Methods and Procedures. To acquire the IED, EED, and DED inside specimens at different unloading points (see Figure 1), a series of SCLUC tests were conducted on an Instron1346 testing machine. The test procedures, using the stress-strain curve of specimen RS-CB-4 as an example, were as follows:

- (1) To attain the uniaxial compressive strength (UCS) of specimens and further to determine the unloading points for SCLUC tests, the UC test was first carried out, and the loading rate was 150 kN/min (1.00 MPa/s) under the force control.
- (2) According to the UCS attained from the first test, five stress unloading points $i\sigma_c^{CB}$ (i represented the setting unloading level, $i = 0.1, 0.3, 0.5, 0.7, 0.9$; σ_c^{CB} represented the UCS of the cuboid specimen in the UC test) were generally set for five specimens, respectively. Then, the SCLUC tests were conducted. As Figure 1 shows, the stress was initially loaded to the unloading point and then unloaded to a minor value of “0.02 $i\sigma_c^{CB}$ ” (due to the restriction of equipment characteristics, the achievable stress minimum for unloading operation was unable to be “0”). After that, the stress was loaded once again from the minor value, until the specimen failed.

Therein, the loading rate and unloading rate were both controlled at 150 kN/min.

- (3) The UCS of the cuboid specimen in the SCLUC tests was denoted by σ_c^{iCB} , then the actual unloading level (i_a^{CB}) can be calculated as follows:

$$i_a^{CB} = \frac{i\sigma_c^{CB}}{\sigma_c^{iCB}} \quad (1)$$

In terms of the cylindrical specimens, a similar test procedure was employed referring to that of the cuboid specimens, except for the loading rate as well as the unloading rate at 120 kN/min (1.02 MPa/s), were adopted. Besides, for the distinction, σ_c^{CL} and σ_c^{iCL} were used to represent the UCS of the cylindrical specimens in the UC and SCLUC tests, respectively.

2.3. Calculation Method of Energy inside Rock Specimens. Considering the specimen volume in test results, the energy density was used as an investigation value in this study. During testing, the energy densities including IED, EED, and DED were commonly utilized to describe failure process of rock specimens. According to the law of thermodynamics which states there is no energy conversion between the rock specimens and the environment during the loading and unloading process [29], the relationship existing among energy densities is described as follows:

$$u_o = u_e + u_d, \quad (2)$$

where u_o is the IED, u_e is the EED, and u_d is the DED.

In this study, different stress unloading points were preset for the SCLUC tests. The initial loading curve and the unloading curve can be precisely determined according to the experimental data at each unloading point, and the energy densities were calculated by the graphical integration according to these curves. As Figure 2(a) shows, at the unloading point, the IED was described as the area enclosed by the loading curve and horizontal axis, and the EED as the area within the unloading curve and horizontal axis. The DED can be determined by subtracting the EED from IED further. Moreover, the calculation methods of IED at the peak point (peak IED) and failure energy density (FED) are shown in Figure 2(b), wherein the FED represented the additional energy provided by further compression of the rock specimen after the peak point. The peak IED was described as the area enclosed by the envelope curve of the two loading curves and horizontal axis, and the FED as the area enveloped by the post-peak curve and horizontal axis.

$$u_o^i = \int_0^{\varepsilon_2} f_1(\varepsilon) d\varepsilon, \quad (3)$$

$$u_e^i = \int_{\varepsilon_1}^{\varepsilon_2} f_2(\varepsilon) d\varepsilon, \quad (4)$$

$$u_d^i = u_o^i - u_e^i, \quad (5)$$

TABLE 1: Basic parameters of specimens.

Specimen shape	Specimen ID	Diameter or width (mm)	Height (mm)	Weight (g)	Density ($\text{g}\cdot\text{cm}^{-3}$)	Longitudinal wave velocity ($\text{m}\cdot\text{s}^{-1}$)
Cylinder	RS-CL-1	48.73	100.80	457	2.43	3360.00
	RS-CL-2	48.72	99.65	455	2.45	3349.58
	RS-CL-3	48.70	99.73	455	2.45	3329.88
	RS-CL-4	48.72	100.33	456	2.44	3305.77
	RS-CL-5	48.70	100.33	458	2.45	3424.23
	RS-CL-6	48.70	100.03	456	2.45	3419.83
Cuboid	RS-CB-1	50.23	100.10	622	2.46	3309.09
	RS-CB-2	50.27	100.19	629	2.48	3295.72
	RS-CB-3	50.30	100.20	629	2.48	3206.40
	RS-CB-4	50.53	100.57	636	2.48	3357.60
	RS-CB-5	50.07	100.31	622	2.47	3378.41
	RS-CB-6	50.18	100.32	625	2.47	3429.74
	RS-CB-7	50.25	100.12	621	2.46	3354.10

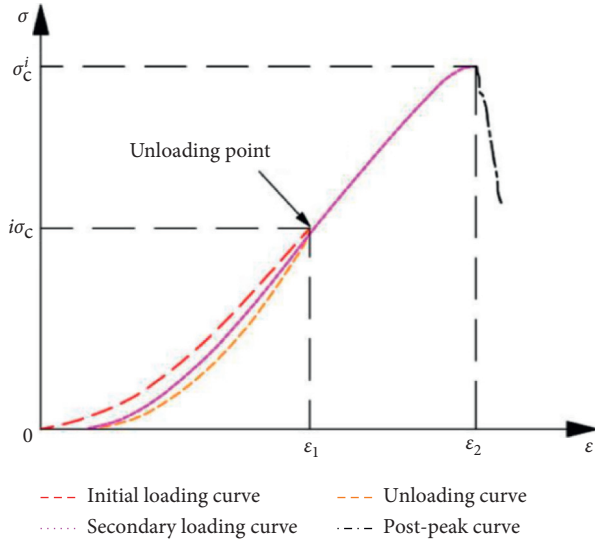


FIGURE 1: Stress-strain path of the SCLUC test.

$$U_o = \int_0^{\varepsilon_1} f_3(\varepsilon) d\varepsilon, \quad (6)$$

$$U_a = \int_{\varepsilon_1}^{\varepsilon_2} f_4(\varepsilon) d\varepsilon, \quad (7)$$

where u_o^i , u_c^i , u_d^i denoted the IED, EED, and DED at the unloading point, respectively; U_o denoted the peak IED, U_a denoted the FED; $f_1(\varepsilon)$, $f_2(\varepsilon)$ denoted the functions of loading and unloading curves, respectively; $f_3(\varepsilon)$ denoted the function of the envelope before peak point; and $f_4(\varepsilon)$ denoted the function of the post-peak curve.

3. Test Results

3.1. Stress-Strain Curves and UCS. To ensure that the measured strain only comes from the specimen, we have subtracted the strain of the stiff pad when drawing the stress-strain curve. The stress-strain curves of cylindrical and cuboid specimens at each unloading level are illustrated in

Figure 3. All the curves were in favourable consistency and generally consisted of a crack closure phase, linear elastic deformation and stable fracture propagation phase, unstable fracture propagation phase, and postfracture phase [30]. Meanwhile, as the stress-strain curves show, the initial loading curves did not coincide with the unloading curves, which was caused by the irreversible permanent deformation occurred in the loading-unloading process [31, 32]. Furthermore, the cuboid specimen possesses a more obvious nonlinear phase near the peak point of the stress-strain curve than the cylindrical specimens.

The UCS of the cylindrical and cuboid specimens in UC and SCLUC tests is shown in Table 2 and Figure 4. The UCS of the cuboid specimens was higher than that of the cylindrical specimens in general and approximately 12 MPa higher on average. Some scholars reported similar results, i.e., the cuboid specimen had a slightly higher strength than the cylindrical specimen by the laboratory test and numerical study [27, 28].

Zhao et al. [27] carried out the UC tests with cuboid specimens (at a size of $50 \times 50 \times 100$ mm, the cross-sectional area was 2500 mm^2) and cylindrical specimens (at a size of $\Phi 50 \times 100$ mm, the cross-sectional area was 1963 mm^2), and the result showed the UCS of the cuboid specimens was approximately 4 MPa higher than that of the cylindrical ones. Based on the basic parameters and sizes of the rock specimen adopted from the laboratory test of Zhao et al., Xu and Cai conducted a numerical simulation with cuboid and cylindrical specimens [28]. The simulation result was consistent with the laboratory test result, namely, the UCS of the cuboid specimens was higher than that of the cylindrical specimens. In such a case, if the cross-section of the cuboid specimen was equivalent to a circle, the equivalent diameter of this circle was 56.4 mm, which was significantly larger than the diameter of the cross-section of the cylindrical specimen. Therefore, a further numerical simulation, where the side length of the cuboid specimen was 44 mm (the cross-sectional area was 1936 mm^2), was conducted, and the result showed a close UCS for the specimens with two shapes. Hence, it can be understood that the cross-sectional areas may exert an influence on the UCS of the two shaped

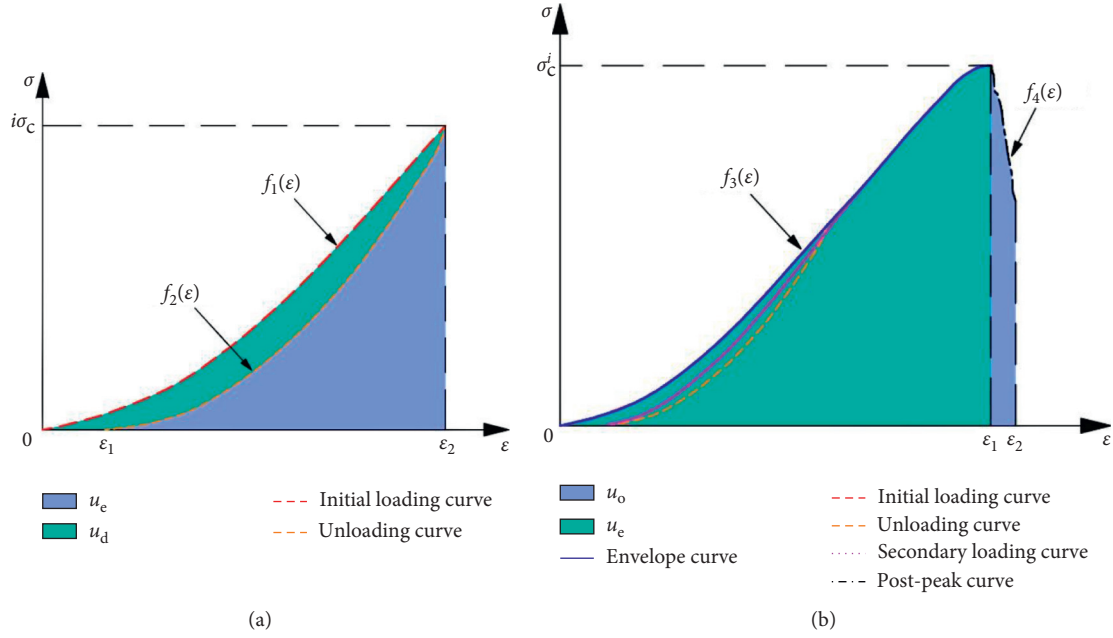


FIGURE 2: Calculation method of energy density. (a) Calculation of energy density at unloading point. (b) Calculation of energy density at peak point.

specimens, and the difference in UCS for the two shaped specimens can be narrowed via equalizing the cross-sectional areas. Xu and Cai confirmed that the end effect controlled the strength of the specimen according to the simulation model [28].

3.2. Energy Evolution Laws inside Specimens. In the rock test, the deformation and failure of the specimen under the action of external force are continuously transformed with the external energy, and the energy distribution and transformation run through the whole process. In recent years, the study of rock failure from an energy viewpoint has become a new research trend, and a host of advances have been obtained [16, 24, 33–36]. Rockburst hazard is one of the dynamic failure phenomena. To more effectively evaluate the rockburst proneness degree of the cylindrical and cuboid specimens further, the energy evolution characteristics inside specimens were explored. According to the energy calculation method in Figure 2(a), the energy densities at different unloading points are calculated in Table 3.

Figure 5 shows the mutual relationship among the IED (u_o^{CL} and u_o^{CB}), EED (u_e^{CL} and u_e^{CB}), DED (u_d^{CL} and u_d^{CB}), and the actual unloading level for cylindrical and cuboid specimens. Figure 5(a) displays the distinctly quadratic relationships between the three types of energy densities and the actual unloading level. For each of the shaped specimens, as the actual unloading level increases, the EED shows a quicker growing rate than the DED, which implies that the energy stored in the specimens was higher than the dissipated energy before the specimens failed. In addition, the fitting functions are displayed in Table 4, and all the fitting correlation coefficients were in excess of 0.9840.

Figures 5(b) and 5(c) display the linear relationships between the three types of energy densities. The largest correlation coefficient was up to 0.9999, which suggested the prominent linearity between the EED, DED, and IED. In addition, no matter what the fitting lines described the relationship between the IED and EED or between the IED and DED, these fitting lines of the two shaped specimens almost coincided. The uniform fitting functions of the linear relationships between the EED, DED, and the IED are as follows:

$$\begin{aligned} u_e &= Au_o + c, \\ u_d &= Bu_o - c, \\ A + B &= 1, \end{aligned} \quad (8)$$

where the A , B , and c are the fitting parameters. According to the fitting functions between the EED (or DED) and IED, we observed that the intercept (c) was 3 orders of magnitude smaller than the corresponding slope (A or B), so the effect of intercept on the linear relationships can be ignored, and the result of the fitting function was chiefly determined by the fitting slope. Of these, the linear relationships were defined as linear energy storage and dissipation laws; the slopes (A and B) of the linear energy storage and dissipation laws were defined as energy storage coefficient and energy dissipation coefficient, respectively, which were indicated the energy storage and dissipation capacities of rocks, respectively [16, 24]. In this study, the energy storage coefficients were 0.7596 and 0.7486, and the energy dissipation coefficients were 0.2404 and 0.2514 for cylindrical and cuboid specimens, respectively, which had little change. Namely, the change of specimen shape had a rare effect on the energy storage and dissipation

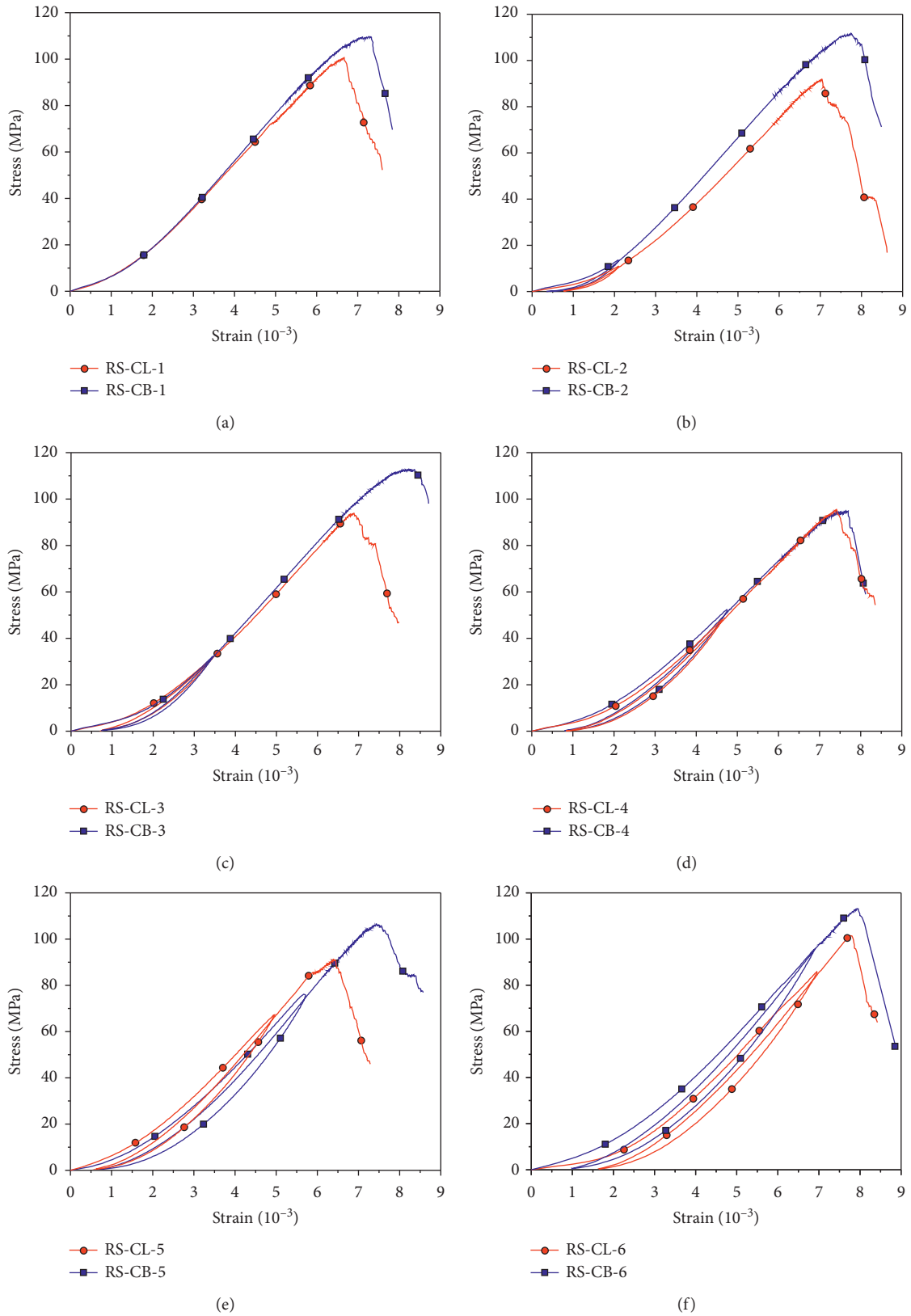


FIGURE 3: Stress-strain curves of cylindrical and cuboid specimens. (a) UC test. (b) $i = 0.1$. (c) $i = 0.3$. (d) $i = 0.5$. (e) $i = 0.7$. (f) $i = 0.9$.

TABLE 2: UCS of cylindrical and cuboid specimens.

Specimen shape	Specimen ID	Compressive strength (MPa)	Average (MPa)
Cylinder	RS-CL-1	100.66	95.76
	RS-CL-2	91.91	
	RS-CL-3	93.89	
	RS-CL-4	95.51	
	RS-CL-5	91.13	
	RS-CL-6	101.47	
Cuboid	RS-CB-1	108.77	107.68
	RS-CB-2	110.52	
	RS-CB-3	111.55	
	RS-CB-4	94.97	
	RS-CB-5	106.42	
	RS-CB-6	112.40	
	RS-CB-7	109.13	

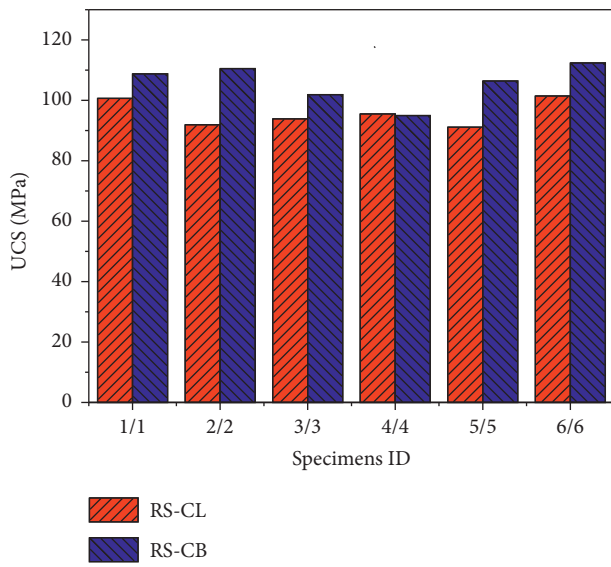


FIGURE 4: UCS of cylindrical and cuboid specimens.

capacities of the red sandstone. In other words, the linear energy storage and dissipation laws had no concern with the specimen shape and were the intrinsic nature of rock materials. Hence, according to the linear energy storage and dissipation laws, the EED and DED at each point can be calculated by using the IED at any corresponding point of the stress-strain curve. Especially, when the u_o^i denoted the peak IED, the EED and DED at the peak point (peak EED and peak DED) of each specimen can be calculated easily and accurately, namely,

$$U_e = AU_o + c, \quad (9)$$

$$U_d = BU_o - c, \quad (10)$$

where U_o , U_e , U_d are the peak IED, peak EED, and peak DED, respectively. These results of the peak EED and peak DED of cylindrical and cuboid specimens are shown in Table 5, as well as the results of the FED. For specimens with the same shape, the energy densities at the peak points were diverse. However, for the same kind of energy density at the specimen peak point, the energy density minimum of the

cuboid specimens was higher than the maximum of the cylindrical specimens. For example, the minimum EED for the cuboid specimens was $0.2344 \text{ mJ}\cdot\text{mm}^{-3}$, which was higher than the maximum of the cylindrical specimens that was $0.2221 \text{ mJ}\cdot\text{mm}^{-3}$.

The reason why the quadratic fitting curves of cuboid specimens are above to those of the cylindrical specimens (in Figure 5(a)) can be explained using the linear energy storage and dissipation laws. Because of the higher strength of the cuboid specimens than that of the cylindrical ones, whilst at the same unloading level, the unloading point of the cuboid specimens was higher than that of the cylindrical specimens. Therefore, according to the energy calculation method, the IED can be calculated in a larger area for cuboid specimens than cylindrical specimens, and the IED of cuboid specimens was larger than that of cylindrical specimens, so the IED curve of cuboid specimens was fitted higher than that of cylindrical specimens further. Meanwhile, due to the energy storage or dissipation coefficients of the two shaped specimens were almost equal, the EED or the DED of the cuboid specimens was larger than that of the cylindrical ones at the same unloading level, and the EED or the DED curve of the cuboid specimens was higher than the curves of cylindrical specimens further.

3.3. Failure Characteristics of Rock Specimens. Using a high-speed camera, the bursting moments of the specimens were recorded. The processes with the same unloading level are contrastively illustrated in Figure 6. The time interval between every two images was annotated as 8 ms for every specimen. Taking the results of the UC tests as examples to show the burst process (as shown in Figures 6(a) and 6(b)). For specimen RS-CL-1, before bursting, a microfracture occurred and a handful of rock fragments slid down near the specimen. Afterward, the specimen burst with a slight voice, and in the meantime, the microfracture expanded and the fragments as well as grains ejected to the ramp below at a slow velocity. For specimen RS-CB-1, the rock block had loosened from the specimen matrix before bursting. Soon, considerable amounts of rock blocks and fragments as well as grains quickly ejected in an approximately horizontal direction.

TABLE 3: Calculation results of energy density.

Specimen shape	Specimen ID	Unloading point (MPa)	Actual unloading level	At unloading point		
				IED ($\text{mJ}\cdot\text{mm}^{-3}$)	EED ($\text{mJ}\cdot\text{mm}^{-3}$)	DED ($\text{mJ}\cdot\text{mm}^{-3}$)
Cylinder	RS-CL-1	—	—	—	—	—
	RS-CL-2	11.03	0.12	0.0085	0.0048	0.0037
	RS-CL-3	30.98	0.33	0.0396	0.0301	0.0095
	RS-CL-4	47.76	0.50	0.0812	0.0608	0.0204
	RS-CL-5	66.52	0.73	0.1353	0.1020	0.0333
	RS-CL-6	86.25	0.85	0.2136	0.1617	0.0519
Cuboid	RS-CB-1	—	—	—	—	—
	RS-CB-2	13.26	0.12	0.0109	0.0065	0.0044
	RS-CB-3	31.23	0.28	0.0395	0.0281	0.0114
	RS-CB-4	52.02	0.55	0.0940	0.0696	0.0244
	RS-CB-5	76.62	0.72	0.1682	0.1268	0.0414
	RS-CB-6	94.42	0.84	0.2611	0.1979	0.0632
	RS-CB-7	103.67	0.95	0.3054	0.2247	0.0807

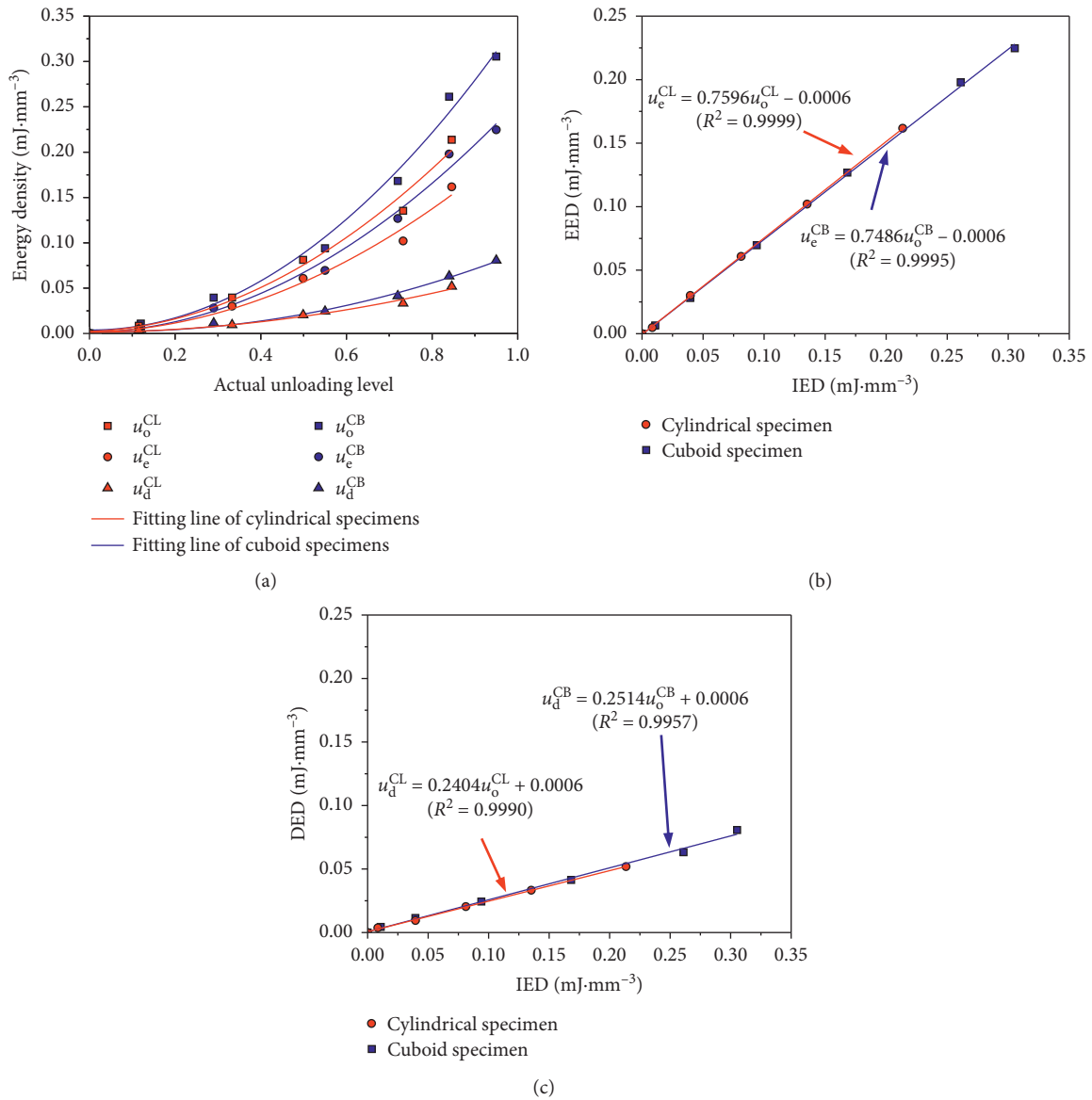


FIGURE 5: Comparison of energy characteristics inside cylindrical and cuboid specimens.

TABLE 4: Fitting functions among three types of energy densities and the actual unloading level.

Relationship	Cylindrical specimen	Cuboid specimen
u_o and i_a	$u_o^{CL} = 0.2582i_a^2 + 0.0178i_a + 0.0022$ ($R^2 = 0.9846$)	$u_o^{CB} = 0.3574i_a^2 - 0.0166i_a + 0.0048$ ($R^2 = 0.9924$)
u_e and i_a	$u_e^{CL} = 0.1970i_a^2 + 0.0128i_a + 0.0012$ ($R^2 = 0.9844$)	$u_e^{CB} = 0.2621i_a^2 - 0.0072i_a + 0.0023$ ($R^2 = 0.9905$)
u_d and i_a	$u_d^{CL} = 0.0612i_a^2 + 0.0051i_a + 0.0011$ ($R^2 = 0.9841$)	$u_d^{CB} = 0.0952i_a^2 - 0.0094i_a + 0.0025$ ($R^2 = 0.9926$)

TABLE 5: Calculations of the energy density.

Specimen shape	Specimen ID	At peak point			FED ($\text{mJ}\cdot\text{mm}^{-3}$)
		IED ($\text{mJ}\cdot\text{mm}^{-3}$)	EED ($\text{mJ}\cdot\text{mm}^{-3}$)	DED ($\text{mJ}\cdot\text{mm}^{-3}$)	
<i>Cylinder</i>	RS-CL-1	0.2932	0.2221	0.0711	0.0755
	RS-CL-2	0.2556	0.1936	0.0620	0.0942
	RS-CL-3	0.2605	0.1973	0.0632	0.0795
	RS-CL-4	0.2829	0.2143	0.0686	0.0697
	RS-CL-5	0.2506	0.1898	0.0608	0.0615
	RS-CL-6	0.2904	0.2200	0.0704	0.0536
<i>Cuboid</i>	RS-CB-1	0.3562	0.2661	0.0901	0.0696
	RS-CB-2	0.3680	0.2749	0.0931	0.0753
	RS-CB-3	0.3913	0.2923	0.0990	0.0657
	RS-CB-4	0.3139	0.2344	0.0795	0.0379
	RS-CB-5	0.3331	0.2488	0.0843	0.0969
	RS-CB-6	0.3707	0.2769	0.0938	0.0817
	RS-CB-7	0.3951	0.2952	0.0999	0.0549

Given the limited space available, the bursting processes of other specimens were not reported in detail here. In addition, the failure mode and burst characteristics of each rock specimen are shown in Figure 7 and Table 6. For failure mode, the cylindrical specimens showed a mainly tensile failure, while most cuboid specimens showed a shear failure. In the simulation conducted by Xu and Cai [28], the granite cylindrical and cuboid specimens both showed the shear failure, which were inconsistent with our test results of red sandstone specimens. The differences may be caused by the different composition, arrangement, and cementation of rock particles inside different lithological rocks. Besides, the specimens with the same shape showed the different failure modes in our study, for example, the specimen RS-CB-1 showed a shear failure, but the specimen RS-CB-4 showed a tensile failure, which was influenced by the anisotropy of specimens.

In fact, for the shear failure of specimens, the microcracks inside the rocks continued to grow and nucleate under the external loads and formed the macroscopic shear plane as approaching the peak strength, which eventually led to the rock failure; for the tensile failure, the axial compression was accompanied by lateral expansion, which was conducive to the development of longitudinal microcracks; after these microcracks reached a certain length, the microcrack propagation became unstable, resulting in axial splitting [37].

Moreover, for the tests with same specimen shape but at different unloading levels, or the tests at a constant unloading

level but with different specimen shapes, the burst characteristics of specimens performed some differences. For example, specimen RS-CB-3 (the cuboid-shaped specimen at the unloading point of 0.3) exhibited the rock block flying out and a mass of fragments ejected at a fast velocity, while only a handful of fragments ejected at a relatively slow velocity for specimen RS-CB-6 (the cuboid-shaped specimen at the unloading point of 0.9); specimen RS-CL-2 (the cylindrical-shaped specimen at the unloading point of 0.1) just burst with fragments falling, while specimen RS-CB-2 (the cuboid-shaped specimen at the unloading point of 0.1) burst with fast fragments ejection. But on the whole, the cylindrical specimens emitted a slight sound at burst moment, and the minor quantity of fragments was ejected at a slow velocity, while the cuboid specimens emitted a louder sound, and a greater quantity of fragments was ejected with a faster velocity.

4. Rockburst Proneness Analysis

4.1. The Elastic Energy Index. The elastic energy index (W_{ET}) proposed by Kidybiński was extensively used in the rock mechanics field. The index is determined by the ratio of elastic energy to dissipated energy being at 80%~90% of peak strength. Accordingly, the values of W_{ET} for specimens RS-CL-6 and RS-CB-6 are 3.16 and 3.13, respectively. From the classification criteria as follows, the red sandstone specimens shaped as cylinder and cuboid performed the same burst proneness, i.e., the low rockburst proneness.

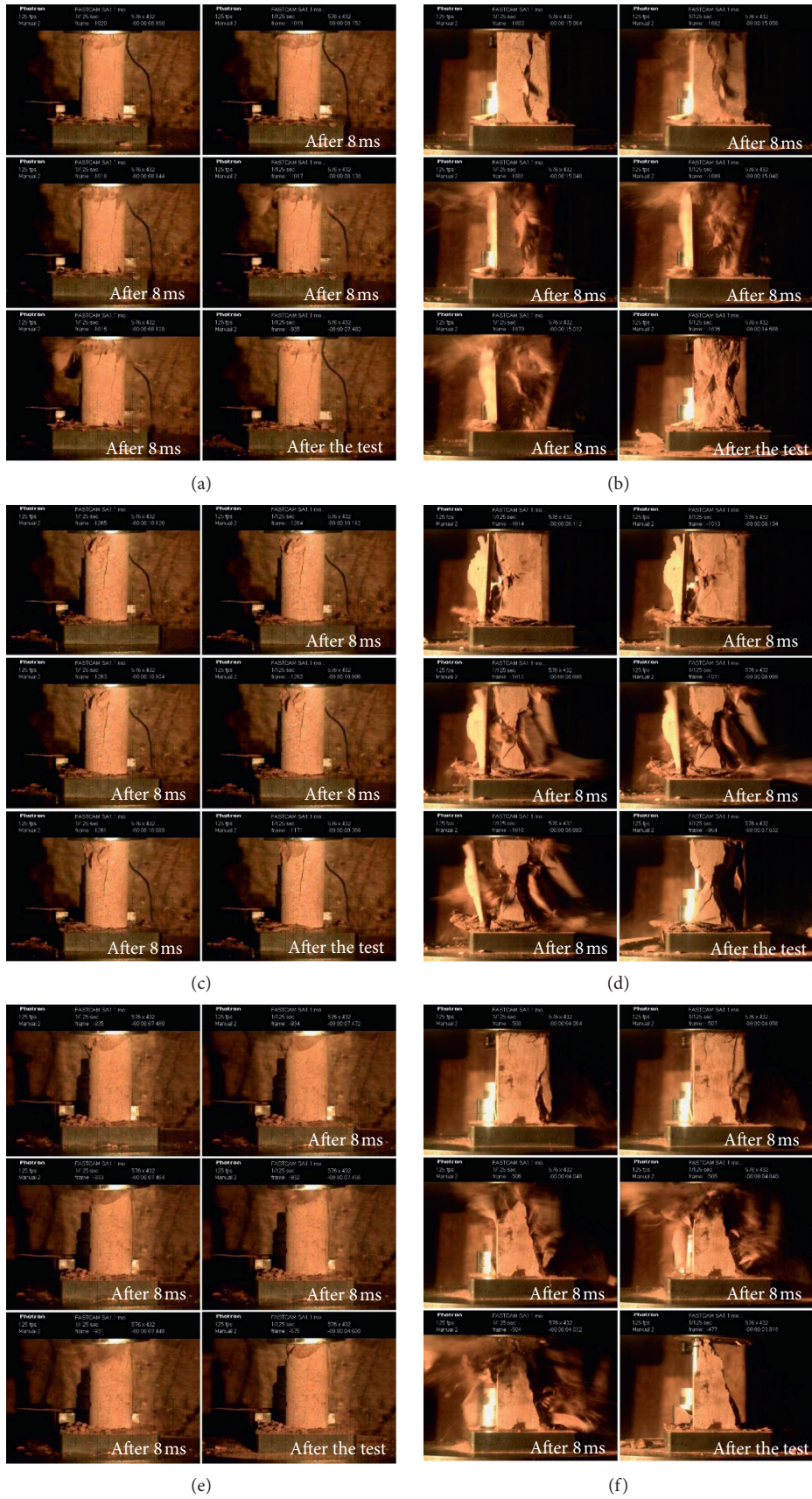


FIGURE 6: Continued.



(g)

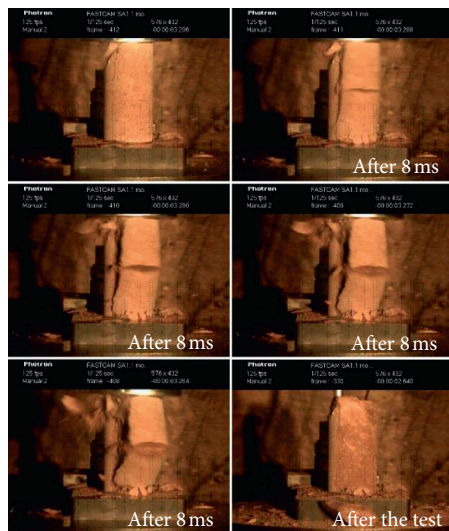
(h)



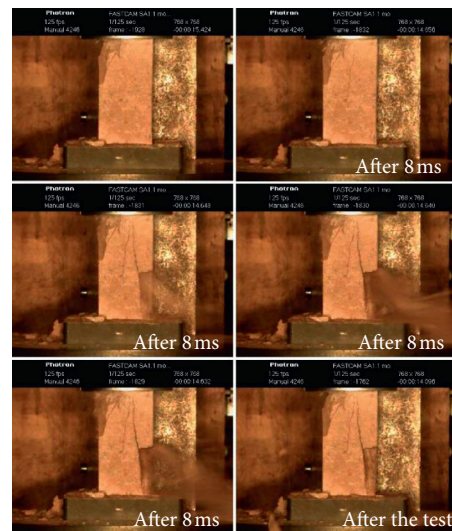
(i)



(j)



(k)



(l)

FIGURE 6: Failure process of specimens with uniaxial compression tests. (a) RS-CL-1. (b) RS-CB-1. (c) RS-CL-2. (d) RS-CB-2. (e) RS-CL-3. (f) RS-CB-3. (g) RS-CL-4. (h) RS-CB-4. (i) RS-CL-5. (j) RS-CB-5. (k) RS-CL-6. (l) RS-CB-6.

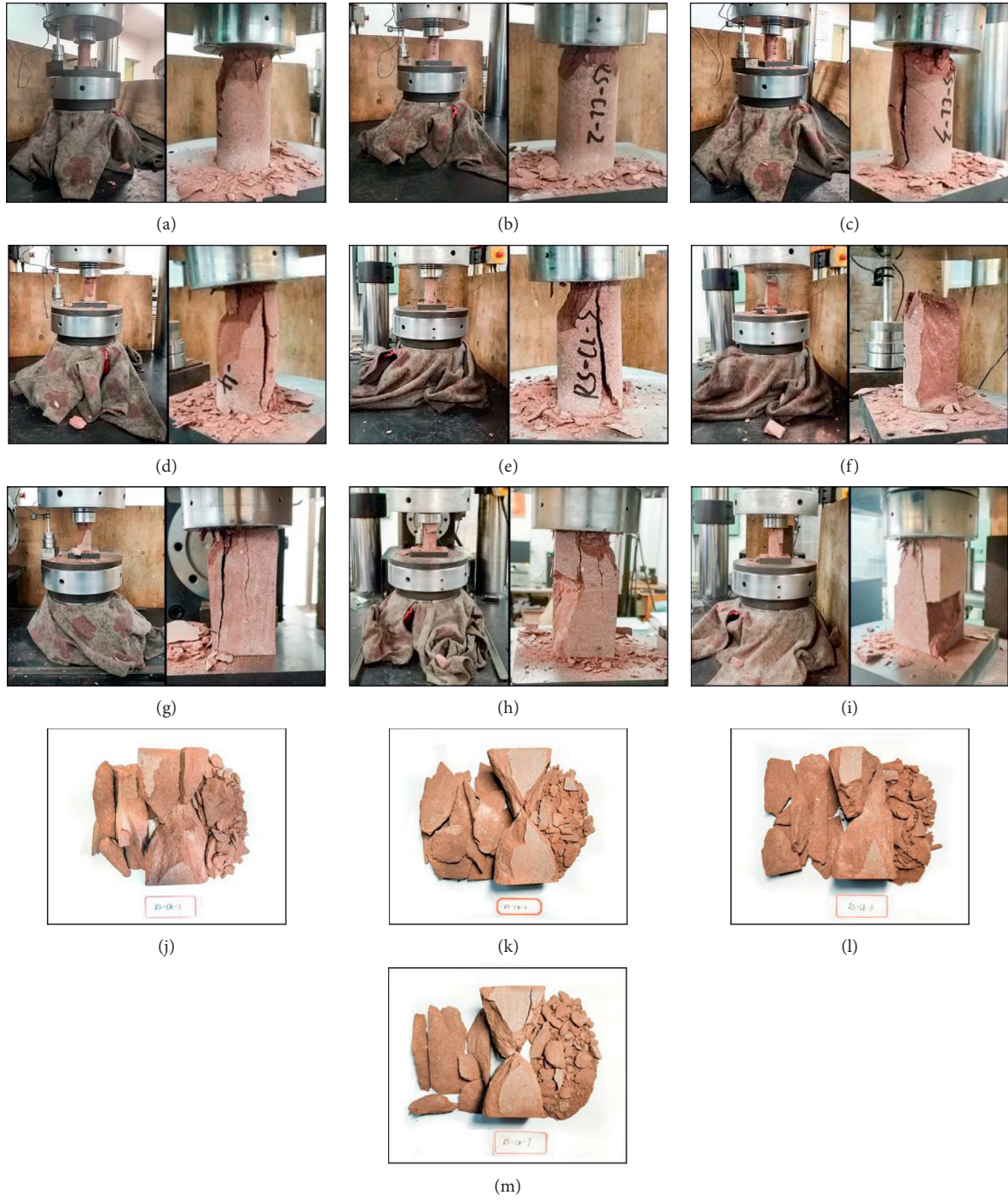


FIGURE 7: Failure characteristics of cylindrical and cuboid specimens. (a) RS-CL-1. (b) RS-CL-2. (c) RS-CL-3. (d) RS-CL-4. (e) RS-CL-5. (f) RS-CL-6. (g) RS-CB-4. (h) RS-CB-5. (i) RS-CB-6. (j) RS-CB-1. (k) RS-CB-2. (l) RS-CB-3. (m) RS-CB-7.

$$W_{ET} \begin{cases} < 2, & \text{no rockburst proneness,} \\ = 2 \sim 5, & \text{low rockburst proneness,} \\ > 5, & \text{high rockburst proneness.} \end{cases} \quad (11)$$

4.2. *The Residual Elastic Energy Index.* According to the obtained linear energy storage law of rock under uniaxial compression [16, 24, 35], Gong et al. [16] proposed the residual elastic energy index (A_{EF}), which was a novel

TABLE 6: Ejection characteristic information of specimens.

Specimen shape	Specimen ID	Failure mode	Burst sound	Fragments ejection velocity	Fragments ejection quantity
<i>Cylinder</i>	RS-CL-1	Tensile	Slight	Slow	Minor
	RS-CL-2	Tensile	Slight	—	—
	RS-CL-3	Tensile and shear	Slight	Slow	Minor
	RS-CL-4	Tensile and shear	Slight	Slow	Modest
	RS-CL-5	Tensile	Slight	Slow	Minor
	RS-CL-6	Tensile and shear	Slight	Slow	Modest
<i>Cuboid</i>	RS-CB-1	Shear	Loud	Fast	Great
	RS-CB-2	Shear	Loud	Medium	Modest
	RS-CB-3	Shear	Loud	Fast	Great
	RS-CB-4	Tensile	Moderate	Slow	Modest
	RS-CB-5	Shear and tensile	Moderate	Medium	Modest
	RS-CB-6	Tensile	Moderate	Medium	Modest
	RS-CB-7	Shear	Loud	Fast	Great

method to estimate rockburst proneness. The calculation method of A_{EF} is as follows:

$$A_{EF} = U_e - U_a, \quad (12)$$

where U_a can be calculated by equation (7), and U_e can be calculated by equation (9). Additionally, the classification criteria of A_{EF} are as follows:

$$A_{EF} \begin{cases} < 50 \frac{\text{kJ}}{\text{m}^3}, & \text{no rockburst proneness,} \\ = 50 \sim 150 \frac{\text{kJ}}{\text{m}^3}, & \text{light rockburst proneness,} \\ = 150 \sim 200 \frac{\text{kJ}}{\text{m}^3}, & \text{moderate rockburst proneness,} \\ > 200 \frac{\text{kJ}}{\text{m}^3}, & \text{strong rockburst proneness.} \end{cases} \quad (13)$$

The A_{EF} values of different shaped specimens are given in Table 7, and the comparative results are shown in Figure 8. According to the classification criteria, most of the cylindrical specimens showed light rockburst proneness, yet the cuboid specimens were moderate and strong in rockburst proneness. Meanwhile, on average for A_{EF} , the cylindrical specimens belonged to light rockburst proneness, yet the cuboid specimens reached to strong rockburst proneness, which indicated the rockburst proneness of cylindrical specimens was lighter than cuboid ones in general.

4.3. The Far-Field Ejection Mass Ratio. Rockburst in deep engineering is a dynamic failure phenomenon. Studying the kinetic energy of the rock fragments after the rock failure in a laboratory test was effective to analyze the rockburst proneness. If the accurate kinetic energy of the ejected rock fragment was required, the ideal was to obtain the mass and velocity of all rock fragments. However, in the UC test, the rock fragments will be ejected into various directions and

angles. We cannot accurately track the path of all rock fragments to measure their speed and mass.

Even so, the faster the speed of the rock fragments was, the farther the ejection distance will be, and the more the mass of the rock fragment ejected into a farther distance will be, the stronger rockburst proneness the specimen showed. Therefore, Gong et al. divided the inner and outer regions according to the boundary of the equipment indenter, and the fragment mass in the two regions was counted, respectively (shown as in Figure 9), and then the rockburst proneness index named far-field ejection mass ratio (M_F) was proposed [16]. The calculation method of M_F is as follows:

$$M_F = \frac{m_1}{(m_1 + m_2)}, \quad (14)$$

where m_1 denotes the fragment mass falling in the area that is outside the indenter and within the test platform; m_2 denotes the fragment mass on the indenter; and the sum of m_1 and m_2 is the fragment mass separated from the specimen matrix. Significantly, because the velocity and distance of the ejected rock fragments were considered, the M_F can manifest the kinetic energy of the fragments to some extent.

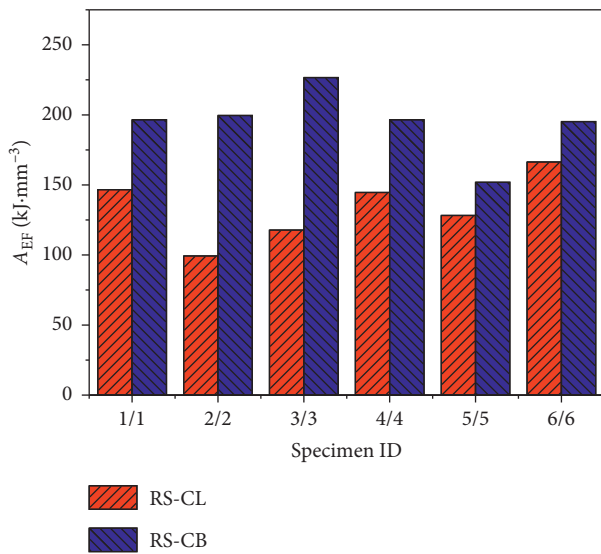
The classification criteria of M_F are as follows:

$$M_F = \begin{cases} = 0, & \text{no rockburst proneness,} \\ = 0 \sim 0.4, & \text{light rockburst proneness,} \\ = 0.4 \sim 0.6, & \text{moderate rockburst proneness,} \\ > 0.6, & \text{strong rockburst proneness.} \end{cases} \quad (15)$$

According to the definition and classification criteria of M_F , two extreme phenomena may exist: (1) when $m_1 = 0$, no fragment mass flies beyond the indenter, under this circumstance, $M_F = 0$, which corresponds to no rockburst proneness; (2) when $m_2 = 0$, all the fragments fly beyond the indenter; in this case, $M_F = 1$, which corresponds that the rock specimen tested is subject to strongest rockburst proneness. When $0 < M_F < 1$, the rockburst proneness degree was in the range from light rockburst proneness to strong rockburst proneness. Table 8 lists the calculations of M_F in this work.

TABLE 7: Calculations of the residual elastic energy index of specimens.

Specimen shape	Specimen ID	A_{EF} ($\text{kJ}\cdot\text{mm}^{-3}$)	Rockburst proneness	Average of A_{EF} ($\text{kJ}\cdot\text{mm}^{-3}$)
Cylinder	RS-CL-1	146.6	Light	133.83
	RS-CL-2	99.4	Light	
	RS-CL-3	117.8	Light	
	RS-CL-4	144.6	Light	
	RS-CL-5	128.3	Light	
	RS-CL-6	166.4	Moderate	
Cuboid	RS-CB-1	196.5	Moderate	200.94
	RS-CB-2	199.6	Moderate	
	RS-CB-3	226.6	Strong	
	RS-CB-4	196.5	Moderate	
	RS-CB-5	151.9	Moderate	
	RS-CB-6	195.2	Moderate	
	RS-CB-7	240.3	Strong	

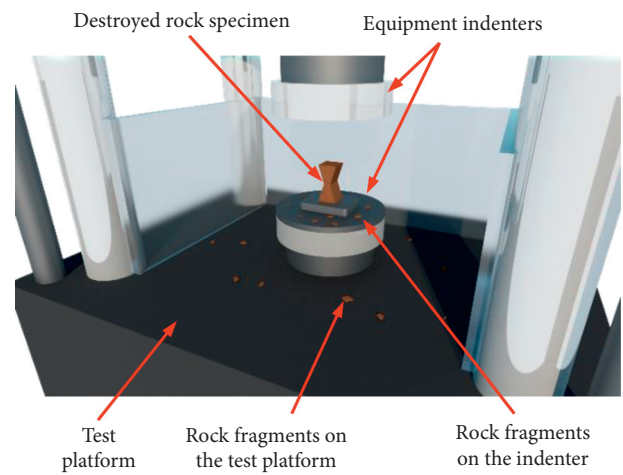
FIGURE 8: Comparative results of cylindrical and cuboid specimens with A_{EF} .

According to the results, the cylindrical specimens performed mainly light and moderate rockburst proneness, yet the cuboid specimens performed moderate and strong proneness on the whole. On average for M_F , the cylindrical specimens were light rockburst proneness, yet the cuboid specimens were strong rockburst proneness.

5. Discussions

In this paper, three indexes (the W_{ET} , A_{EF} , and M_F) were adopted to access the rockburst proneness of red sandstone specimens with two shapes, respectively. However, the discriminations of three indexes had some discrepancies: W_{ET} indicated that the cylindrical and cuboid specimens showed the same low rockburst proneness; A_{EF} and M_F indicated the cylindrical specimens showed the light rockburst proneness, yet the cuboid specimens showed the moderate and strong rockburst proneness in general.

To compare the accuracy of the discriminant results of two shaped specimens by the three rockburst proneness indexes, we analyzed the discriminant mechanism of them.

FIGURE 9: Calculation schematic of M_F .

At first, we took the maximal peak IED of two shaped specimens (in Table 5) as the maximal value (for example, the maximal peak IED of the cylindrical specimen was $0.2932 \text{ mJ}\cdot\text{mm}^{-3}$). By bringing the IED from 0 to $0.2932 \text{ mJ}\cdot\text{mm}^{-3}$ into the linear energy storage and dissipation laws of the cylindrical specimen, the EED and DED corresponding to the IED at each point in the pre-peak phase of the stress-strain curve can be calculated, and the ratio of EED to DED corresponding to the IED at each point can be calculated further. Hence, the variations of the ratio of EED to DED versus IED can be shown in Figure 10. Besides, the ratio results attained from the actual tests are also demonstrated as the discrete points in Figure 10 as well.

In Figure 10, the discrete points were well distributed near the variations of energy density ratio for specimens of each shape, and the discreteness of discrete points of the cuboid specimens was apparently smaller than that of the cylindrical specimens. Besides, as the IED increased, the energy density ratio tended to rise up sharply at first and then quickly became nearly steady. The ratio increased extremely slowly when the IED exceeded $0.20 \text{ mJ}\cdot\text{mm}^{-3}$. With the IEDs reaching to their maximums (i.e., at the peak strength), the energy density ratios for cylindrical and cuboid specimens are 3.12 and 2.95, respectively, which show

TABLE 8: Calculations of the far-field ejection mass ratio of specimens.

Specimen shape	Specimen ID	M_F	Rockburst proneness	Average of M_F
Cylinder	RS-CL-1	0.47	Moderate	0.30
	RS-CL-2	0.04	Light	
	RS-CL-3	0.15	Light	
	RS-CL-4	0.43	Moderate	
	RS-CL-5	0.14	Light	
	RS-CL-6	0.59	Moderate	
Cuboid	RS-CB-1	0.76	Strong	0.64
	RS-CB-2	0.48	Moderate	
	RS-CB-3	0.71	Strong	
	RS-CB-4	0.58	Moderate	
	RS-CB-5	0.55	Moderate	
	RS-CB-6	0.54	Moderate	
	RS-CB-7	0.86	Strong	

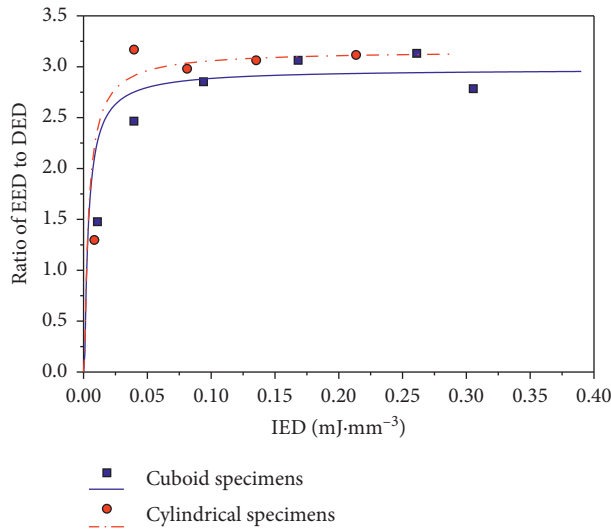


FIGURE 10: Relationship between IED and the ratio of EED to DED.

the rockburst proneness of the two shaped specimens being the low proneness and are consistent with the assessments by W_{ET} . From this viewpoint, W_{ET} had certain validity. Unexpectedly, according to the failure phenomena of the specimens accorded by a high-speed camera, the rockburst proneness of the cylindrical specimen was significantly lighter than that of the cuboid specimen.

In fact, the evaluation results of the W_{ET} (or the method which used the ratio of EED to DED at the peak strength in this paper) did not consider the post-peak phase, and it cannot reflect the energy dissipation required for the failure of the rock after the peak strength and the energy release after the rock failure. Moreover, the laboratory rockburst phenomenon of the rock specimen only occurred when the applied stress reaches the peak strength, which also indicated that the assessment of the rockburst proneness of the specimen via the W_{ET} had certain limitations.

Since the UCS of the cuboid specimen was greater than that of the cylindrical specimen in general, more energy needed to be input into the cuboid specimen to reach its peak point, so the peak IED of the cuboid specimen will be

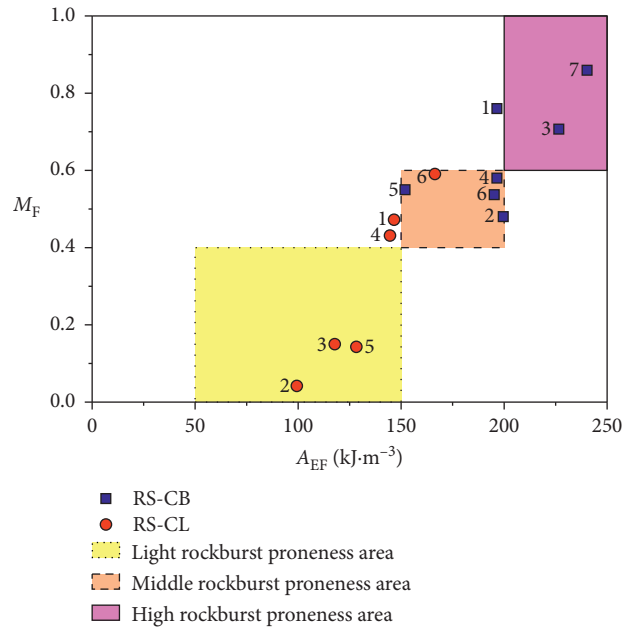


FIGURE 11: Matching relationship between the residual elastic energy index and far-field ejection mass ratio.

greater than that of the cylindrical specimen. Moreover, due to the energy storage coefficients for the cuboid and cylindrical specimens were roughly constant, the peak EED of the cuboid specimen was larger than that of the cylindrical specimen. Besides, Gong et al. [16] have found that no connection existed between the peak EED and FED. The residual EED was mainly determined by the peak EED. According to the calculations of the energy densities at the peak point (in Table 5), the peak EED of the cylindrical specimen was always smaller than that of the cuboid specimen, so the residual EED of the cylindrical specimen will be smaller than that of the cuboid specimen in general. Thus, the cylindrical specimen showed a lighter rockburst proneness than the cuboid specimen, which was in close accordance with the failure phenomena of both cylindrical and cuboid specimens. Namely, the A_{EF} was more suitable than the W_{ET} to assess the rockburst proneness of specimens.

Moreover, the rockburst proneness of the two shaped specimens was evaluated from the kinetic energy of ejected rock fragments through the M_F in this work, and the results also conform to the actual burst phenomena, namely, the cylindrical specimen showed the light rockburst proneness, and the cuboid specimen showed the moderate and strong rockburst proneness. Figure 11 illustrates the matching area of corresponding rockburst proneness degree between the A_{EF} and M_F . It shows that the rockburst proneness estimated results from cylindrical and cuboid specimens were at or near the same matching areas. In other words, the rockburst proneness estimated results calculated by the A_{EF} and M_F were in good accordance, and these two methods can accurately assess the rockburst proneness of specimens.

In fact, the A_{EF} assessed the rockburst proneness of rock materials via a qualitative method from the energy conversion perspective, and the M_F was a semiquantitative method that considered the failure characteristics. If A_{EF} and M_F are combined to evaluate the rockburst proneness, the evaluation results may be more accurate.

6. Conclusions

Based on the results attained from the UC and SCLUC tests with cylindrical and cuboid specimens, a comparison study of the specimen shape effect on rockburst proneness of the red sandstone was carried out. The following conclusions were drawn:

- (1) The development paths of the stress-strain curves change little with the changing specimen shapes. Meanwhile, the UCS of the cuboid specimens was approximately 12 MPa higher than that of the cylindrical specimens. Equalizing the stressed areas of the two shaped specimens would narrow the difference in UCS.
- (2) For either cylindrical or cuboid specimens, significant energy laws occur during the loading and unloading process. On the one hand, any of the IED, EED, or DED presents distinctly quadratic functional relationships with the increment of the actual unloading level. On the other hand, the prominent linear law occurs between the EED, DED, and IED. Moreover, the energy storage coefficient and energy dissipation coefficient are barely affected by the change in specimen shape.
- (3) For the failure mode, the cylindrical specimens show a principally tensile failure, and the cuboid specimens show a shear failure. Moreover, for the tests with same specimen shapes but at different unloading levels, or the tests at a constant unloading level but with different specimen shapes, the specimens show the different burst characteristics that are slight or strong. But on the whole, the cylindrical specimen emitted a slight sound, and its ejected fragments are slow and minor, while the cuboid specimen mostly performed a louder sound, and a

greater quantity of fragments was ejected at a faster velocity.

- (4) The rockburst proneness of every specimen is evaluated by the elastic energy index (W_{ET}), the residual elastic energy index (A_{EF}), and the far-field ejection mass ratio (M_F). Of these, the calculation results of the W_{ET} are different from the actual burst phenomena, yet the results of A_{EF} and M_F are in favourable agreement and in accordance with the burst phenomena that the cylindrical specimens show a light rockburst proneness, while the cuboid specimens show a moderate or strong rockburst proneness on the whole.

Nomenclature

m_1 :	Rock fragment mass that is outside the indenter and on the test platform (g)
m_2 :	Rock fragment mass on the indenter (g)
U_a :	Failure energy density after the peak point ($\text{mJ}\cdot\text{mm}^{-3}$)
u_d :	Dissipated energy density ($\text{mJ}\cdot\text{mm}^{-3}$)
u_d^{CL} and u_d^{CB} :	Dissipated energy density of cylindrical and cuboid specimens ($\text{mJ}\cdot\text{mm}^{-3}$)
u_e :	Elastic energy density ($\text{mJ}\cdot\text{mm}^{-3}$)
u_e^{CL} and u_e^{CB} :	Elastic energy density of cylindrical and cuboid specimens ($\text{mJ}\cdot\text{mm}^{-3}$)
u_e^i :	Elastic energy density at the unloading point ($\text{mJ}\cdot\text{mm}^{-3}$)
U_e :	Elastic energy density at the peak point ($\text{mJ}\cdot\text{mm}^{-3}$)
u_d^i :	Dissipated energy density at the unloading point ($\text{mJ}\cdot\text{mm}^{-3}$)
u_o :	Input energy density ($\text{mJ}\cdot\text{mm}^{-3}$)
u_o^{CL} and u_o^{CB} :	Input energy density of cylindrical and cuboid specimens ($\text{mJ}\cdot\text{mm}^{-3}$)
u_o^i :	Input energy density at the unloading point ($\text{mJ}\cdot\text{mm}^{-3}$)
U_o :	Input energy density at the peak point ($\text{mJ}\cdot\text{mm}^{-3}$)
$\sigma_c^{\text{CL}}, \sigma_c^{\text{CB}}$:	Uniaxial compressive strength of cylindrical and cuboid specimens in the UC test (MPa)
$\sigma_c^{i\text{CL}}, \sigma_c^{i\text{CB}}$:	Uniaxial compressive strength of cylindrical and cuboid specimens in the SCLUC test (MPa)
<i>Dimensionless</i>	
A_{EF} :	Residual elastic energy index
DED:	Dissipated energy density
EED:	Elastic energy density
FED:	Failure energy density
i :	Setting unloading level in the SCLUC test
i_a^{CL} and i_a^{CB} :	Actual unloading level of cylindrical and cuboid specimens in the SCLUC test
IED:	Input energy density
M_F :	Far-field ejection mass ratio
SCLUC:	Single-cycle loading-unloading uniaxial compression
UC:	Uniaxial compression
UCS:	Uniaxial compressive strength
W_{ET} :	Elastic energy index

W_p^{ET} : Peak-strength strain energy storage index.

Data Availability

All data generated or analyzed during this study are included within this article.

Conflicts of Interest

The authors declare that there are no conflicts of interest regarding the publication of this paper.

Acknowledgments

This work was supported by the National Natural Science Foundation of China (Grant no. 41877272) and the State Key Laboratory for GeoMechanics and Deep Underground Engineering, China University of Mining & Technology, Beijing (Grant no. SKLGDUEK1827).

References

- [1] W. D. Ortlepp and T. R. Stacey, "Rockburst mechanisms in tunnels and shafts," *Tunnelling and Underground Space Technology*, vol. 9, no. 1, pp. 59–65, 1994.
- [2] P. K. Kaiser and M. Cai, "Design of rock support system under rockburst condition," *Journal of Rock Mechanics and Geotechnical Engineering*, vol. 4, no. 3, pp. 215–227, 2012.
- [3] C. P. Lu, G. J. Liu, H. Y. Wang, and J. H. Xue, "Numerical investigation of rockburst effect of shock wave on underground roadway," *Shock and Vibration*, vol. 2015, Article ID 867582, 10 pages, 2015.
- [4] P. G. Ranjith, J. Zhao, M. Ju, R. V. S. De Silva, T. D. Rathnaweera, and A. K. M. S. Bandara, "Opportunities and challenges in deep mining: a brief review," *Engineering*, vol. 3, no. 4, pp. 546–551, 2017.
- [5] X. B. Li, F. Q. Gong, M. Tao et al., "Failure mechanism and coupled static-dynamic loading theory in deep hard rock mining: a review," *Journal of Rock Mechanics and Geotechnical Engineering*, vol. 9, no. 4, pp. 767–782, 2017.
- [6] C. P. Lu, Y. Liu, N. Zhang, T. B. Zhao, and H. Y. Wang, "In-situ and experimental investigations of rockburst precursor and prevention induced by fault slip," *International Journal of Rock Mechanics and Mining Sciences*, vol. 108, pp. 86–95, 2018.
- [7] X. T. Feng, Y. Y. Zhou, and Q. Jiang, "Rock mechanics contributions to recent hydroelectric developments in China," *Journal of Rock Mechanics and Geotechnical Engineering*, vol. 11, no. 3, pp. 511–526, 2019.
- [8] P. K. Kaiser and S. M. Maloney, "Scaling laws for the design of rock support," *Seismicity Associated with Mines, Reservoirs and Fluid Injections*, vol. 150, no. 3-4, pp. 415–434, 1997.
- [9] X. F. Si and F. Q. Gong, "Strength-weakening effect and shear-tension failure mode transformation mechanism of rockburst for fine-grained granite under triaxial unloading compression," *International Journal of Rock Mechanics and Mining Sciences*, vol. 131, Article ID 104347, 2020.
- [10] A. Manouchehrian and M. Cai, "Simulation of unstable rock failure under unloading conditions," *Canadian Geotechnical Journal*, vol. 53, no. 1, pp. 22–34, 2016.
- [11] F. q. Gong, Y. Luo, X. B. Li, X. F. Si, and M. Tao, "Experimental simulation investigation on rockburst induced by spalling failure in deep circular tunnels," *Tunnelling and Underground Space Technology*, vol. 81, pp. 413–427, 2018.
- [12] F. Q. Gong, X. F. Si, X. B. Li, and S. Y. Wang, "Experimental investigation of strain rockburst in circular caverns under deep three-dimensional high-stress conditions," *Rock Mechanics and Rock Engineering*, vol. 52, no. 5, pp. 1459–1474, 2019.
- [13] H. Wagner, "Deep mining: a rock engineering challenge," *Rock Mechanics and Rock Engineering*, vol. 52, no. 5, pp. 1417–1446, 2019.
- [14] M. He, L. Ribeiro e Sousa, T. Miranda, and G. Zhu, "Rockburst laboratory tests database—application of data mining techniques," *Engineering Geology*, vol. 185, pp. 116–130, 2015.
- [15] C. S. Ma, W. Z. Chen, X. J. Tan, H. M. Tian, J. P. Yang, and J. X. Yu, "Novel rockburst criterion based on the TBM tunnel construction of the Neelum–Jhelum (NJ) hydroelectric project in Pakistan," *Tunnelling and Underground Space Technology*, vol. 81, pp. 391–402, 2018.
- [16] F. Q. Gong, J. Y. Yan, and X. B. Li, "A new criterion of rock burst proneness based on the linear energy storage law and the residual elastic energy index," *Chinese Journal of Rock Mechanics and Engineering*, vol. 37, no. 9, pp. 1993–2014, 2018.
- [17] M. Cai and P. K. Kaiser, *Rockburst Support Reference Book—Volume I: Rockburst Phenomenon and Support Characteristics*, MIRARCO, Laurentian University, Greater Sudbury, Canada, 2018.
- [18] A. Kidybiński, "Bursting liability indices of coal," *International Journal of Rock Mechanics and Mining Sciences*, vol. 18, no. 4, pp. 295–304, 1981.
- [19] S. P. Singh, "Burst energy release index," *Rock Mechanics and Rock Engineering*, vol. 21, no. 2, pp. 149–155, 1988.
- [20] J. A. Wang and H. D. Park, "Comprehensive prediction of rockburst based on analysis of strain energy in rocks," *Tunnelling and Underground Space Technology*, vol. 16, no. 1, pp. 49–57, 2001.
- [21] A. Mazaira and P. Konicek, "Intense rockburst impacts in deep underground construction and their prevention," *Canadian Geotechnical Journal*, vol. 52, no. 10, pp. 1426–1439, 2015.
- [22] M. F. Cai, "Prediction and prevention of rockburst in metal mines—a case study of Sanshandao gold mine," *Journal of Rock Mechanics and Geotechnical Engineering*, vol. 8, no. 2, pp. 204–211, 2016.
- [23] W. Y. Guo, T. B. Zhao, Y. L. Tan, F. H. Yu, S. C. Hu, and F. Q. Yang, "Progressive mitigation method of rock bursts under complicated geological conditions," *International Journal of Rock Mechanics and Mining Sciences*, vol. 96, pp. 11–22, 2017.
- [24] F. Q. Gong, J. Y. Yan, X. B. Li, and S. Luo, "A peak-strength strain energy storage index for rock burst proneness of rock materials," *International Journal of Rock Mechanics and Mining Sciences*, vol. 117, pp. 76–89, 2019.
- [25] B. C. Haimson and C. Chang, "A new true triaxial cell for testing mechanical properties of rock, and its use to determine rock strength and deformability of westerly granite," *International Journal of Rock Mechanics and Mining Sciences*, vol. 37, no. 1-2, pp. 285–296, 2000.
- [26] C. D. Ma, X. B. Li, F. Chen, and J. C. Xu, "Fracturing behavior study of biaxial compression of rock subjected to dynamic disturbance load," *Chinese Journal of Rock Mechanics and Engineering*, vol. 29, no. 6, pp. 1238–1244, 2010.
- [27] X. G. Zhao, M. Cai, J. Wang, and P. F. Li, "Strength comparison between cylindrical and prism specimens of Beishan granite under uniaxial compression," *International Journal of Rock Mechanics and Mining Sciences*, vol. 76, pp. 10–17, 2015.
- [28] Y. H. Xu and M. Cai, "Numerical study on the influence of cross-sectional shape on strength and deformation behaviors

- of rocks under uniaxial compression,” *Pure and Applied Geophysics*, vol. 84, pp. 129–137, 2017.
- [29] H. P. Xie, Y. Ju, and L. Y. Li, “Criteria for strength and structural failure of rocks based on energy dissipation and energy release principles,” *Chinese Journal of Rock Mechanics and Engineering*, vol. 24, no. 17, pp. 3003–3010, 2005.
- [30] Z. T. Bieniawski, “Mechanism of brittle fracture of rock: part I—theory of the fracture process,” *International Journal of Rock Mechanics and Mining Sciences & Geomechanics Abstracts*, vol. 4, no. 4, pp. 395–406, 1967.
- [31] R. W. Zimmerman, “The effect of microcracks on the elastic moduli of brittle materials,” *Journal of Materials Science Letters*, vol. 4, no. 12, pp. 1457–1460, 1985.
- [32] J. C. Jaeger, N. G. W. Cook, and R. W. Zimmerman, *Fundamentals of Rock Mechanics*, Blackwell Publishing, Malden, MA, USA, 4th edition, 2007.
- [33] R. Peng, Y. Ju, J. G. Wang, H. Xie, F. Gao, and L. Mao, “Energy dissipation and release during coal failure under conventional triaxial compression,” *Rock Mechanics and Rock Engineering*, vol. 48, no. 2, pp. 509–526, 2015.
- [34] B. G. Tarasov and T. R. Stacey, “Features of the energy balance and fragmentation mechanisms at spontaneous failure of class I and class II rocks,” *Rock Mechanics and Rock Engineering*, vol. 50, no. 10, pp. 2563–2584, 2017.
- [35] F. Q. Gong, S. Luo, and J. Y. Yan, “Energy storage and dissipation evolution process and characteristics of marble in three tension-type failure tests,” *Rock Mechanics and Rock Engineering*, vol. 51, no. 11, pp. 3613–3624, 2018.
- [36] F. Q. Gong, J. Y. Yan, S. Luo, and X. B. Li, “Investigation on the linear energy storage and dissipation laws of rock materials under uniaxial compression,” *Rock Mechanics and Rock Engineering*, vol. 52, no. 12, pp. 4237–4255, 2019.
- [37] H. Munoz, A. Taheri, and E. K. Chanda, “Fracture energy-based brittleness index development and brittleness quantification by pre-peak strength parameters in rock uniaxial compression,” *Rock Mechanics and Rock Engineering*, vol. 49, no. 12, pp. 4587–4606, 2016.